Acta Geodyn. Geomater., Vol. 16, No. 3 (195), 315–330, 2019
DOI: 10.13168/AGG.2019.0027
journal homepage: https://www.irsm.cas.cz/acta

ORIGINAL PAPER

STRESS ANALYSIS OF FAULT SLIPS DATA RECORDED WITHIN THE DĚDIČNÁ ŠTOLA GALLERY IN THE RYCHLEBSKÉ HORY MTS., NE PART OF THE BOHEMIAN MASSIF

Jakub STEMBERK * [1, 2], Miroslav COUBAL [1, 3], Josef STEMBERK [1] and Petra ŠTĚPANČÍKOVÁ [1]

[1] *Institute of Rock Structure and Mechanics, The Czech Academy of Sciences, V Holešovičkách 94/41, 180 00 Prague 8, Czech Republic*
[2] *Faculty of Science, Charles University, Albertov 6, 128 00 Prague 2, Czech Republic*
[3] *Institute of Geology, The Czech Academy of Sciences, Rozvojová 269, 160 00 Prague 6, Czech Republic*

**Corresponding author's e-mail:* jakub.stemberk@irsm.cas.cz

ARTICLE INFO

Article history:
Received 21 June 2019
Accepted 15 August 2019
Available online 9 September 2019

Keywords:
Active tectonics
3-D fault slip monitoring
Transient fault slip acceleration
Switching stress/strain states

ABSTRACT

This work presents the results of 3-D movements of faults occurring in the Dědičná štola Gallery in the Rychlebské hory Mts. during the period between 2014 and 2017. The faults were monitored by TM-71 extensometers. The detected fault slip is nonlinear and is affected by short transient periods of acceleration. One dominant and a series of minor transient fault slip accelerations were recognised. The recorded accelerations were induced by switching two compressional stress/strain states – WNW-ESE to NW-SE compression corresponding to the stress field of the Western European stress domain and to NNE-SSW corresponding to the stress field of the NW part of the Carpathian stress domain. The extensional state, oriented NW-SE, corresponding to gravitational spreading due to the Rychlebské hory Mts. uplift, was recognised.

1. INTRODUCTION

Rychlebské hory Mts. / Złote Góry Mts., as a part of the north-eastern margin of the Bohemian Massif, represent a mountain ridge along the NW-SE striking Sudetic Marginal Fault (SMF, Fig. 1), which is one of the most important faults in central Europe (e.g. Ivan, 1966; Oberc and Dyjor, 1969; Krzyszkowski et al., 1995; Badura et al., 2003; Štěpančíková et al., 2008). The SMF separates the Fore-Sudetic block to the NE and the Sudetic Mts. to the SW (Fig. 1). As a part of EU-TecNet (see www.tecnet.cz), a series of TM-71 high-resolution, 3-D extensometers (Košťák, 2006; Klimeš et al., 2012) was installed to record the slip along the selected faults identified in the Dědičná štola Gallery (the DG, Fig. 2) in the northern part of the Rychlebské hory Mts. Fault slip data recorded in the period between 2014 and 2017 were analysed to characterise the local recent tectonic regime. The results are discussed particularly in the light of possible exogenous and endogenous effects that could affect the fault slip data. Finally, the recorded fault slips were analysed using paleostress methods to determine the recent stress/strain field around the DG. Methodically, we extended the most recent stress state analyses based on fault slips recorded by TM-71 extensometers located in different parts of Europe published by Briestenský et al. (2018), from the Western Carpathians, Stemberk et al. (2019), from the Central Apennines, and from the Eastern Alps, Baroň et al. (2019). As they applied graphical approximation for recognition of recent stress/strain states (c.f. Marrett and Allmendinger, 1990; Allmendinger et al., 2011), according to Málek et al. (1991) we also applied statistical grouping using upgraded ROCK2014 software.

2. GEOLOGICAL AND TECTONIC SETTING

The DG is situated in the western part of the Rychlebské hory Mts. and belongs to the Central Sudetes as a part of the Sudetic Mts. The Sudetic Mts. represent the north-easternmost exposed fragment of the crystalline basement of the Variscan Belt in Europe with a variety of metamorphic complexes with Neoproterozoic, and Lower Palaeozoic to Devonian protoliths (e.g. Mazur et al., 2006; Kroner et al., 2008). It was developed in Devonian and Early Carboniferous as a result of the closure of ocean basins and amalgamation of Armorican terranes, followed by their accretion to the East European Platform (e.g. Franke and Żelaźniewicz, 2000; Aleksandrowski and Mazur, 2002; Kroner et al., 2008). During the Late Cretaceous, the broader area was buried by an up to ~4-7 km thick sea sedimentary cover and rapidly exhumed to near-surface temperatures during the Late Cretaceous–Palaeocene.

Cite this article as: Stemberk J jr, Coubal M, Stemberk J, Štěpančíková P: Stress analysis of fault slips data recorded within Dědičná štola Gallery in the Rychlebské hory Mts., NE part of the Bohemian massif. Acta Geodyn. Geomater., 16, No. 3 (195), 315–330, 2019. DOI: 10.13168/AGG.2019.0027

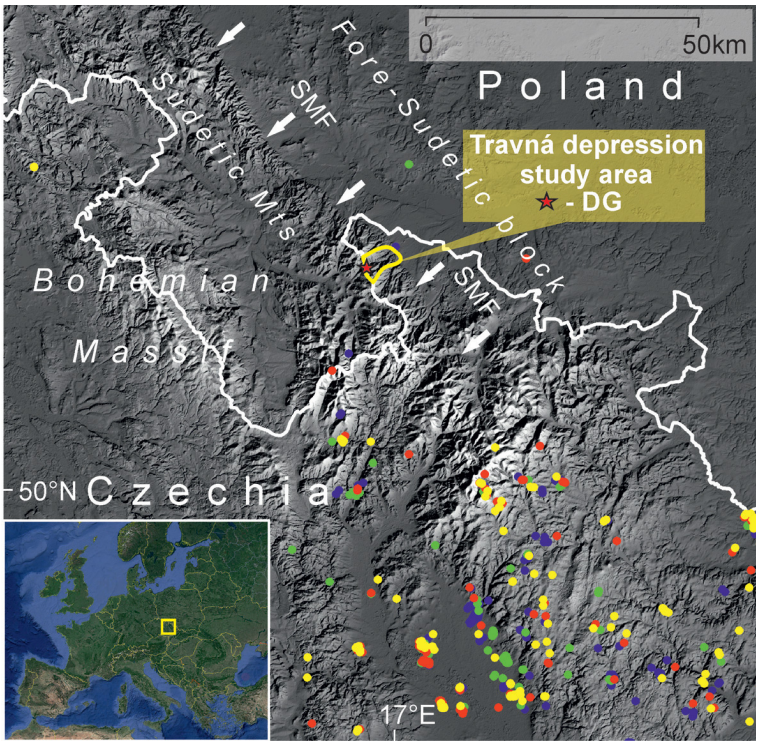

Fig. 1 Topographic relief map of the Central Sudety Mts. using SRTM (resolution 30m; Farr (eds.), 2007) with Travná depression study area; The Sudetic Marginal Fault forms a border between Sudetic Mts. on the SW side and Sudetic Foreland on the NE side. Dots indicate earthquake epicenters recorded by EPI-MONET seismic network (Sýkorová et al., 2018) in years 2014 (blue dot), 2015 (green dot), 2016 (red dot) and 2017 (yellow dot).

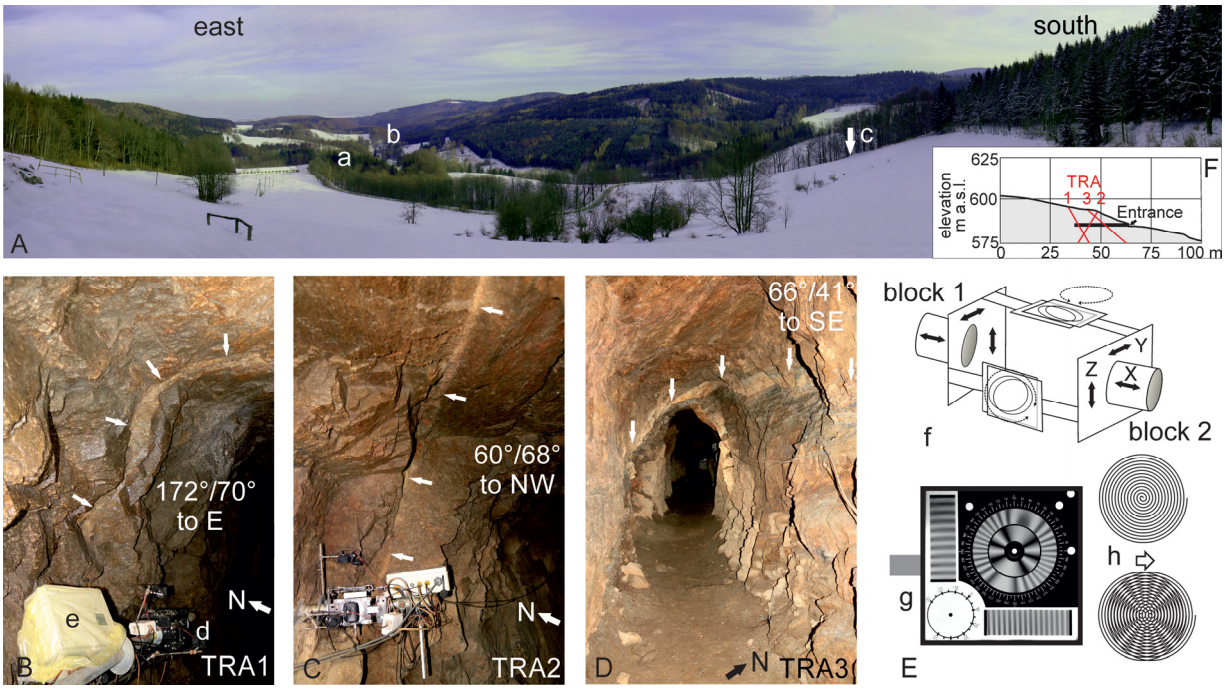

Fig. 2 A – Travná depression developed on ENE-WSW faults; (a) Travná village; (b) Javornický potok brook deeply cut valley; (c) the Dědičná štola Gallery
B – Fault TRA1 (white arrows) fit with (d) the TM-71 device with (e) automatic reading apparatus
C – Fault TRA2
D – Fault TRA3 with well visible fault plane and thick layer of tectonic clay
E – The TM-71 optical mechanical extensometer; the 3-D displacement between the two blocks are inferred from the moiré patterns recorded along three perpendicular planes. (f) Schematic drawing of the TM-71 extensometer. Arrows indicate the possible movements of the components; (g) example of a photograph of a moiré pattern between two glass plates with fine engraved spirals; (h) spiral similar to those of the engraved glass plate of TM-71 (much less dense); Two overlapping concentric spirals displaced with respect to one another. Picture moved horizontally by the distance indicated by the arrow – now the moiré effect is observable.
F – Longitudinal profile in direction WNW-ESE of the hill-slope and the Dědičná štola Gallery

The Sudetic Mts. as well as the Fore-Sudetic block were elevated and eroded, planated surfaces were evolved and partially covered due to Oligocene and Miocene marine transgressions coming from the Central European Basin in the Palaeocene to Eocene (Oberc, 1972). The uplift of the Sudetic block with the formation of the Sudetic Mts. versus the Fore-Sudetic block, began in the Pliocene and continues to date (e.g. Ivan, 1966; Štěpančíková et al., 2008), while the total uplift of the Sudetic Mts. since the Miocene was estimated to be approximately 1200-1500 m (Oberc, 1972; Dyjor, 1983).

In a more detailed scale, the DG is located in the Travná depression (Figs. 2 and 6) of the Pliocene (Ivan, 1966). The depression is developed along faults striking between 70° to 90° and between 340° and 360°. A detailed tectonic setting of the gallery surroundings in Figure 6 summarises all of the proofed or anticipated faults according to Bobula (1968), Brezňan et al. (1957a, 1957b), Don et al. (2003), Ivan (1997), Müller and Čurda (2003), Ondra and Potměšil (1965), Pecina et al. (2005), Skácel (1989) and Skácelová (1992). Unfortunately, there is no more detailed information about the geometry of the faults. Three faults recognised within the DG disrupt the gneiss and para-gneiss rock. The fault planes are filled by a layer of tectonic clay and breccia (Fig. 2) with several noticeable generations of striae. Faults TRA2 and TRA3 are also dominant in terms of morphology. The mountain ridge to the NE of the DG is predisposed by these faults (Fig. 6).

Regarding recent seismic activity, the study area is situated on the boundary of two different seismic areas – the Hronov-Poříčí fault seismic area, with maximum intensity I_0 = IV°-VII° and the Nízký Jeseník seismic area with intensity I_o up to VI°. Detailed studies of the seismological events in the adjacent area were investigated by Havíř et al. (2001), Skácelová and Havíř (1999), Špaček et al. (2008) and Zedník et al. (2013). Focal mechanism analysis indicates the NNW-SSE orientation of the main stress (Špaček et al., 2008). Recently, the study area has been monitored by the IPE-MONET seismic network. The strongest earthquake (*ML*=3.5) since the beginning of the fault slip monitoring was recorded on 10 December 2017 (Sýkorová et al., 2018). The strongest historical earthquake $I_0 = 7^0$ MSK in the broader area, which was also felt in the Rychlebské hory Mts. and surroundings, occurred on 11 June 1895 (Pagaczewski, 1972).

The study area is situated near the border between the Bohemian Massif and the Western Carpathians. A NW-SE stress orientation is more dominant in the Bohemian Massif according to focal mechanism analyses (Grünthal and Stromeyer, 1992; Müller et al., 1992; Peška, 1992; Zoback, 1992; Jarosiński et al., 2006; Vavryčuk et al., 2013; Špaček et al., 2015) and an NNE-SSW orientation of compression is more dominant in the Western Carpathians according to borehole breakout analyses (Jarosiński, 2006).

3. METHODS

3.1. FAULT SLIP MONITORING

As a part of the EU-TecNet (www.tecnet.cz), TM-71 extensometers are used for regular highly precise monitoring of fault slips along selected faults within galleries. The extensometers record both lateral and shear displacement as well as rotations between two blocks separated by a discontinuity (e.g. Košťák, 1969; Klimeš et al., 2012; Martí et al., 2013). All possible relative movements of the blocks are measured with a high accuracy in an order higher than 0.0125 mm (Martí et al., 2013). The limitation and applicability of the extensometers were demonstrated and discussed by Klimeš et al. (2012). The fault slip data, as well as temperature, humidity and air pressure were collected regularly with a daily frequency at 0:00 GMT.

The recorded fault slips are visualised in the Cartesian coordinate system *x, y, z* (Fig. 2). For the fault kinematics and dynamics analyses, the data are recalculated to the coordinate system *s, h, p,* and adapted to monitored fault plane geometry. The *s*-axis represents the dip-slip component with normal (N) or reverse (R) slip sense. The *h*-axis represents the strike-slip component with a dextral (D) or sinistral (S) sense of slip. The *p*-axis is perpendicular to the fault plane and corresponds to the fault contraction or dilatation. The fault plane is described with components A_p (fault strike/trend) and φ_p (fault dip/plunge). The vector sum of the *s* and *h* components is defined as the total slip vector, after adding the *p* component as the total movement vector (Table 1). This form of data set, in contrast with the fault-slip markers (striae), always contains a known sense of the total slip vector as well as a movement component of the normal vector to the fault plane corresponding to contraction or dilatation.

3.2. FAULT SLIP KINEMATICS AND DYNAMICS ANALYSES

All three fault slip vector components *s, h, p* related to the time scales are graphically presented in Figure 3. The recorded events were defined as a time period of unified movement tendency (described by *s*, *h*, *p*-axis) on an individual fault (E1A, E2A, etc. in Fig. 3). The sudden change in movement tendency creates the border between individual events. Similar events were grouped to individual episodes. An episode (P1, T2, etc. in Fig. 3) is defined as a time period when the same stress regime occurred on the monitored faults. The time synchronisation factor of the episodes was taken into account.

3.2.1. FAULT KINEMATICS

The extensometer data, presented in the Cartesian coordinate system as components *s, h, p*, were converted into the polar coordinate system. The total slip vector consists of components A_s (trend) and φ_s (plunge) and is supplemented by the sense of slip (Table 1).

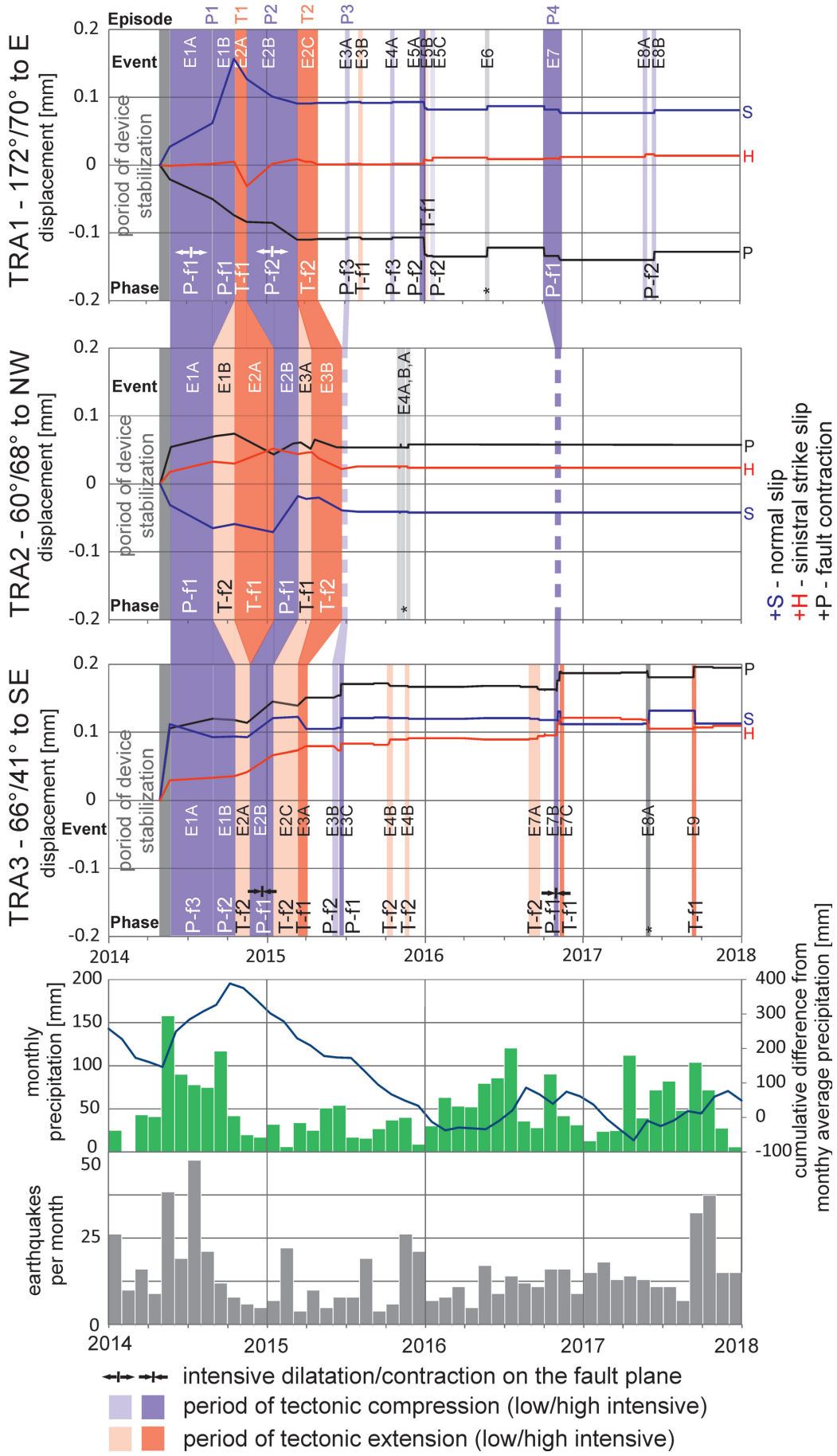

Fig. 3 Cumulative fault slips observed on TRA1-TRA3 during period 2014-2017 with marked events (e.g. E5C, E4A), episodes (e.g. P2, T1) and stress phases (e.g. P-f2, T-f1). Data are compared with monthly and cumulative precipitation and monthly earthquake occurrence during study period.

Table 1 Dataset of recorded events; A_p – fault strike (°); φ_p – fault dip (°); A_s – trend of total vector slip (°); φ_s – plunge of total vector slip (°); Sense of slip: N – normal, R – reverse, S – sinistral, D – dextral; α - misfit angle; * - not assigned event to episode / to stress phase.

			Fault plane		Movement vector			Total slip vector						
Fault	**Event**	**Time period**	**A_p**	**Φ_p**	**S [mm]**	**H [mm]**	**P [mm]**	**A_s**	**Φ_s**	**Sense of slip**	**Total slip [mm]**	**Episode**	**Phase**	**α**
TRA1	**E1A**	May 22, 2014 - Aug 29, 2014	172°	70°E	-0.035	0.003	0.029	96°	69°	R	0.030	**P1**	**P - f1**	**3.9°**
	E1B	Aug 29, 2014 - Oct 18, 2014			-0.095	0.003	0.024	87°	70°	R	0.095	**P1**	**P - f1**	**7.1°**
	E2A	Oct 18, 2014 - Nov 17, 2014			0.030	-0.036	0.01	156°	37°	N	0.047	**T1**	**T - f1**	**7.1°**
	E2B	Nov 17, 2014 - Mar 14, 2015			0.036	0.040	0.026	9°	39°	N	0.054	**P2**	**P - f2**	**23.9°**
	E2C	Mar 14, 2015 - May 5, 2015			-0.001	-0.008	-0.001	354°	7°	R	0.008	**T2**	**T - f2**	**9.9°**
	E3A	Jul 8, 2015 - Jul 9, 2015			-0.001	0.001	-0.002	153°	42°	R	0.001	**P3**	**P - f3**	**3.4°**
	E3B	Aug, 8, 2015 - Aug 11, 2015			0.001	-0.001	0.002	153°	42°	N	0.001	*	**T - f1**	**1.6°**
	E4A	Oct 20, 2015 - Oct 21, 2015			-0.001	0.001	-0.002	153°	42°	R	0.001	*	**P - f3**	**3.4°**
	E5A	Jan 1, 2016 - Jan 3, 2016			0.005	0.007	0.013	6°	33°	N	0.009	*	**P - f2**	**17.4°**
	E5B	Jan 3, 2016 - Jan 9, 2016			0.006	-0.002	0.014	126°	63°	N	0.006	*	**T - f1**	**24.7°**
	E5C	Jan 22, 2016 - Jan 23, 2016			0.000	0.004	0.001	352°	0°	S	0.004	*	**P - f2**	**18.1°**
	E6	May 28, 2016 - May 29, 2016			0.005	0.002	-0.013	33°	61°	N	0.005	*	*	*
	E7	Oct 7, 2016 - Nov 14, 2016			-0.008	0.003	0.018	130°	62°	R	0.009	**P4**	**P - f1**	**12.6°**
	E8A	May 29, 2017 - May 30, 2017			0.000	0.004	0.000	352°	0°	S	0.004	*	**P - f2**	**18.1°**
	E8B	Jun 20, 2017 - Jun 21, 2017			0.002	0.004	-0.012	2°	25°	N	0.004	*	**P - f2**	**8.7°**
TRA2	**E1A**	May 22, 2014 - Aug 29, 2014	60°	68°NW	-0.034	-0.003	0.015	317°	67°	R	0.034	**P1**	**P - f1**	**6.7°**
	E1B	29 Aug, 2014 - Oct 18, 2014			0.006	0.000	-0.003	330°	68°	N	0.006	**T1**	**T - f2**	**22.7°**
	E2A	Oct 18, 2014 - Jan 15, 2015			0.012	0.022	0.022	252°	26°	N	0.025	**T1**	**T - f1**	**15.5°**
	E2B	Jan 15, 2015 - Mar 14, 2015			-0.063	-0.020	-0.008	290°	62°	R	0.066	**P2**	**P - f1**	**5.8°**
	E3A	Mar 14, 2015 - Apr 15, 2015			0.002	0.002	0.003	261°	41°	N	0.003	**T2**	**T - f1**	**1.3°**
	E3B	May 1, 2015 - Jun 24, 2015			0.019	0.009	-0.016	278°	57°	N	0.021	**T2**	**T - f2**	**2.7°**
	E4A	Nov 3, 2015 - Nov 4, 2015			0.001	-0.003	-0.002	53°	17°	N	0.003	*	*	*
	E4B	Nov 5, 2015 - Nov 6, 2015			-0.001	0.003	0.002	53°	17°	R	0.003	*	*	*
	E4C	Nov 23, 2016 - Nov 24, 2016			0.001	-0.003	-0.002	53°	17°	N	0.003	*	*	*
TRA3	**E1A**	May 22, 2014 - Aug 29, 2014	66°	41°SE	-0.019	0.004	-0.014	172°	40°	R	0.019	**P1**	**P - f3**	**6.7°**
	E1B	Aug 29, 2014 - Nov 17, 2014			0.000	0.008	0.006	66°	0°	S	0.008	**P1**	**P - f2**	**20.1°**
	E2A	Oct 18, 2014 - Nov 17, 2014			0.001	0.006	0.004	73°	6°	N	0.006	**T1**	**T - f2**	**13.1°**
	E2B	Nov 17, 2014 - Jan 15, 2015			-0.030	0.032	-0.025	211°	27°	R	0.044	**P2**	**P - f1**	**7.8°**
	E2C	Jan 15, 2015 - Mar 14, 2015			0.002	0.006	0.004	73°	6°	N	0.006	**T2**	**T - f2**	**13.1°**
	E3A	Mar 14, 2015 - Apr 2, 2015			0.018	0.006	-0.012	132°	38°	N	0.019	**T2**	**T - f1**	**3.8°**
	E3B	Jun 6, 2015 - Jun 16, 2015			-0.002	-0.006	-0.003	80°	12°	R	0.006	**P3**	**P - f2**	**1.8°**
	E3C	Jun 22, 2015 - Jun 23, 2015			-0.014	0.010	-0.017	199°	32°	R	0.017	**P3**	**P - f1**	**19.3°**
	E4B	Oct 9, 2015 - Oct 14, 2015			0.001	0.008	0.004	71°	5°	N	0.008	*	**T - f2**	**15.2°**
	E7A	Sep 19, 2016 - Oct 6, 2016			0.002	0.007	0.005	78°	10°	N	0.007	*	**T - f2**	**6.7°**
	E7B	Nov 3, 2016 - Nov 19, 2016			-0.014	0.025	-0.027	223°	19°	R	0.029	**P4**	**P - f1**	**5.9°**
	E7C	Nov 10, 2016 - Nov 14, 2016			0.019	0.009	0.002	124°	36°	N	0.021	*	**T - f1**	**10.5°**
	E8A	May 29, 2017 - Jun 3, 2017			-0.019	-0.013	0.007	114°	33°	R	0.023	*	*	*
	E9	Sep 16, 2017 - Sep 17, 2017			0.015	0.002	-0.019	146°	41°	N	0.015	*	**T - f1**	**7.4°**

$$A_s\left(rad\right) = arctg\left(\frac{h}{\cos\Phi_p * s}\right)$$

$$\Phi_s\left(rad\right) = arctg\sqrt{\left(\frac{s^2 - \left(\cos\Phi_p * s\right)^2}{h^2 + \left(\cos\Phi_p * s\right)^2}\right)}$$

$$total\ slip\ vector = \sqrt{s^2 + h^2}$$

To control find outs, the size of the total slip vector was used to evaluate the size of slip on fault during the individual events. Values above 0.0075 mm/event were marked as highly intensive contraction/dilatation events, and below this value as low intensive events. Moreover, the values of the *p*-axis component, which shows the size of a normal vector to the fault plane, were categorised. Values above 0.025 mm/event were marked as intensive contraction/dilatation on the fault plane (Fig. 3, Table 1).

3.2.2. FAULT DYNAMICS

The two different paleostress methods were applied to data sets of kinematic characteristics on studied faults during a one time-period (episode or event) to determine the orientation of the stress field (Fig. 4). The approximate paleostress method of the P and T-axis was used and the results were visualised in FaultKin7 software (c.f. Marrett and Allmendinger, 1990; Allmendinger et al., 2011). Moreover, for better and more accurate results, the polyphaser analysis numerical method (Angelier, 1994) in the updated ROCK2014 software (Málek et al., 1991) was used.

3.3. STRESS PARAMETER ANALYSES

The paleostress analysis method is based on continuum mechanics, which for the known parameters of stress orientation estimates the orientation of a slip on arbitrary fault planes (Angelier, 1982, 1989). In practice, the inverse situation is solved, where the principal parameters of the stress, which caused the later measured slips on the reactivated faults, are calculated based on the measured orientation of slips on more fault planes. The principal stress parameters are expressed as a total stress tensor. In this work, a reduced stress tensor was calculated, which is an approximation of the total stress tensor neglecting the isotropic part of the crustal stress (Angelier, 1989, 1994). The approximation can be used because the site is located in very shallow parts of the Earth's crust. The reduced stress tensor, which characterises the single stress state, has the following principal parameters: direction of its principal stresses ($\sigma1$– maximum, $\sigma2$ – intermediate and $\sigma3$ – minimum) and ratio $\Phi = (\sigma2-\sigma3) / (\sigma1-\sigma3)$ describing the difference between magnitudes of principal stresses (Angelier, 1994). The values of Φ range from 0 (uniaxial compression) to 1 (uniaxial extension). The Φ ratio parameter varies depending on the amount of data (n) in individual stress phases (Málek et al., 1991). All of the suggested stress phases include less than 10 data sets, the reliability of the Φ ratio is low, but was also taken into consideration. Episodes with sub-horizontal $\sigma1$ were marked as pressure (P1-P4), and episodes with sub-horizontal $\sigma3$ were marked as extensional (T1-T2). The orientation of the principal axis is presented in Table 2.

The misfit angle α (Table 1) between the observed shear direction on the studied fault plane recorded as striae and the theoretical ones, which correspond to a computed stress state, was also calculated (Hippolyte et al., 2012). In this case, striae were not measured directly on the fault plane, but were calculated from the fault slip. In this work, a misfit angle less than 25° is assumed as a good agreement. A heterogeneous data set of striae is divided into homogenous subsets based on a comparison of misfit angles with all individual stress states. All of the data were automatically separated into homogenous subsets in each iteration in the ROCK2014 program (Málek et al., 1991). The reliability and precision of the used method were discussed in e.g. Coubal et al. (2015).

According to the Coulomb criterion, the group of planes, where the normal component is lowest and the shear stress component is the highest, could be activated by a slip during individual stress phases (Morris et al., 1996; Fossen, 2010). There are two planes, which are theoretically-oriented ±45° from $\sigma1$ and transect in $\sigma2$. In practice, due to the influence of the non-synaxial distribution of the normal stress component, the angle between $\sigma1$ and both planes is lower. The angle value of ±30° (Ramsay and Huber, 1987; Fossen, 2010) was used as a good approximation. Similarly, the best orientation to the stress field in individual stress phases has planes with a perpendicular orientation to the $\sigma3$ axis (Ramsay and Lisle, 2000). These planes have a tendency to dilate (Fig. 4).

4. RESULTS

4.1. FAULT SLIP ANALYSES

Site TRA1 (17 m below ground level):

The TRA1 fault strikes 172° and dips 70° to the E (Fig. 2). The general trend of the slips corresponds to a slow sinistral slip with a relative uplift (reverse oblique fault) of the eastern block and fault dilatation. The magnitude of the individual fault slips ranges from 0.01 mm to 0.1 mm (Fig. 3). At the end of 2014, there was a short period when the sense of the slip changed from sinistral to dextral and back. There was also a change in the vertical fault slip component, when the eastern block firstly subsided relatively to the western block (normal slip), and later began to uplift relatively to the western block (thrust). Nevertheless, the slip developed nonlinearly and resulted mostly from one dominant transient event recorded in 2014 and the beginning of 2015 as well as from several minor transient events (Fig. 3).

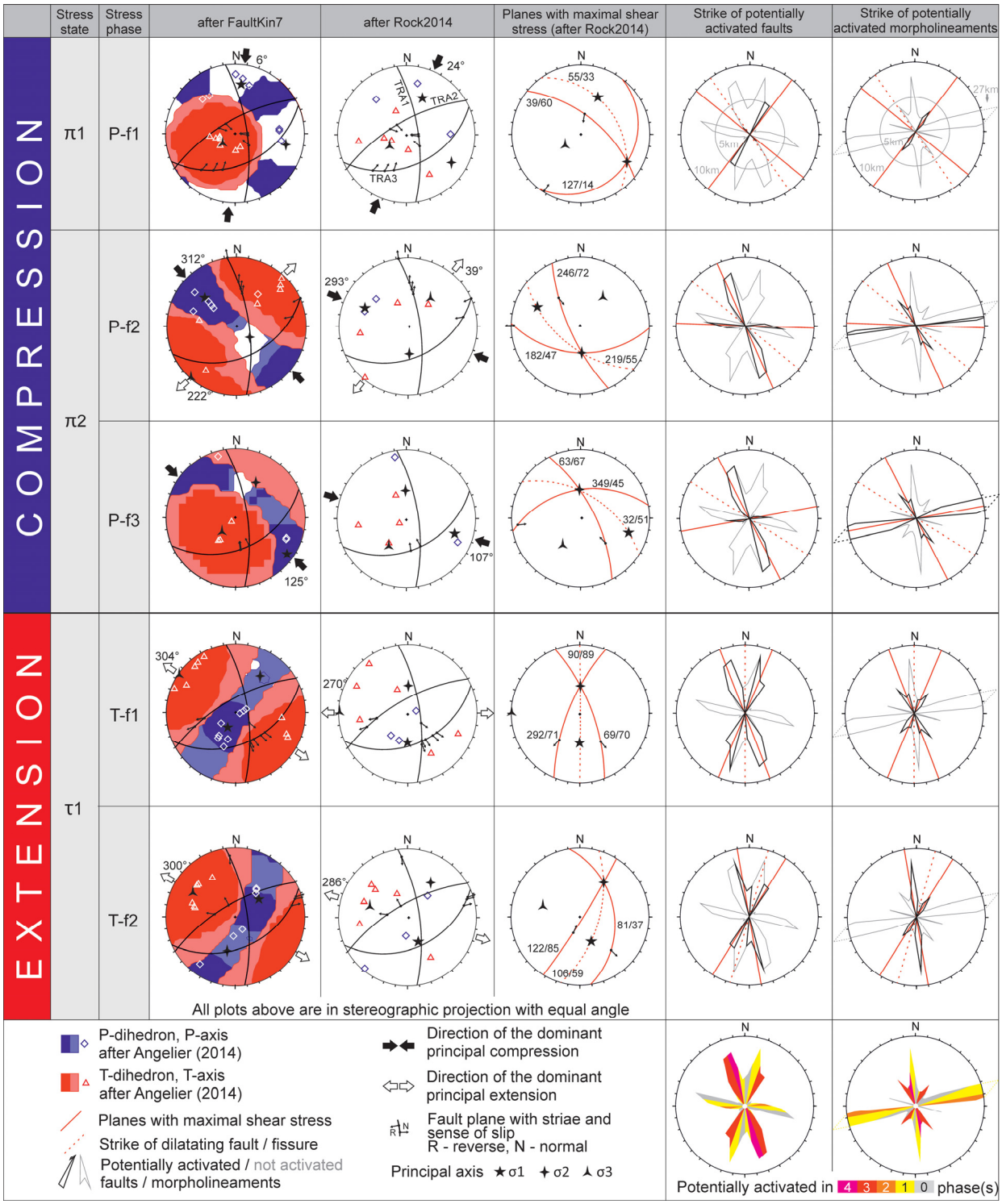

Fig. 4 Results of fault slip dynamics analyses complemented by results of geomorphological analyses.
Overall character of the observed compression and extension phases.
First column: Beach ball charts of the orientation of P-axis and T-axis
and resulting P- and T- dihedrons, constructed for measured fault slips during individual phases visualize in software FaultKin7
Second column: Stereographic plots show the results of polyphaser analysis numerical method (Angelier, 1994), in software ROCK2014 (Málek, 1991)
Third column: Stereographic plot with planes with maximal shear stress (after Ramsay and Huber, 1987; Fossen, 2010) and planes/fissures with high tendency for dilatation (Ramsay and Lisle, 2000)
Fourth column: The radar plot with strikes (10° interval) of potentially activated faults during individual stress phases. The cumulative length of faults in strike intervals is considered.
Fifth column: The radar plot with strikes of potentially activated morpholineaments during individual stress phases. The cumulative length of morpholineaments in strike intervals is considered.

Table 2 Stress phase parameters; Tr. – trend (°); Pl. – plunge (°); Dir. – sense of slip; N – normal; R – reverse; Φ – ratio of stress differences Φ = (σ2- σ3) / (σ1- σ3); n – number of events forming homogenous subset (32 events from 38); Q – quality estimator for fault-slip data subset. The grade of the quality estimator is based on the number of events forming homogenous subset: A – 15 or more events (excellent), B – 10-14 events (good), C – 4-9 events (fair), D – 4 events (poor) (after Coubal et al., 2015).

Stress phase	after FaultKin7						after Rock2014						Φ	n	Q	Planes with maximal shear stress						Dilatating Fissures	
	σ1		σ2		σ3		σ1		σ2		σ3					Plane 1			Plane 2				
	Tr.	Pl.	Tr.	Pl.	Tr.	Pl.	Tr.	Pl.	Tr.	Pl.	Tr.	Pl.				Tr.	Pl.	Dir,	Tr.	Pl.	Dir.	Tr.	Pl.
P-f1	6	18	102	16	232	65	24	29	121	14	235	57	0.663	8	C	39	60	R	127	14	R	55	33
P-f2	312	26	130	64	222	1	293	22	177	47	39	35	0.267	7	C	182	47	N	246	72	R	219	55
P-f3	125	6	32	31	224	59	107	18	358	45	212	39	0.699	4	D	63	67	R	349	45	R	32	51
T-f1	211	64	34	26	304	1	180	44	1	46	270	1	0.199	8	C	69	70	N	292	71	N	90	89
T-f2	53	45	193	37	300	21	157	47	34	27	286	31	0.466	6	C	81	37	N	122	85	R	106	59

Site TRA2 (14 m below ground level):

The TRA2 fault strikes 60° and dips 68° to the NW (Fig. 2). The fault slip was only recorded during the period from 2014 to June 2015. At the beginning of 2015, the slow sinistral strike slip changed to dextral. Moreover, the relative uplift of the NW block towards the SE changed in January 2015 to subsidence of the NW block towards the SE block. The dominant contraction and dilatation switched until June 2015. No slip of the TRA2 fault has been detected since June 2015. The amplitude of the individual movement ranges from 0.01 mm to 0.05 mm (Fig. 3).

Site TRA3 (8 m below ground level):

The TRA3 fault strikes 66° and dips 41° to the SE (Fig. 2D). The fault is the largest recognised fault in the DG. The trend of slip is sinistral with a predominant normal slip and fault contraction. The magnitude of the fault slip events ranges from 0.01 mm to 0.1 mm. The dominant sinistral slip was interrupted by a dominant dextral slip during the period from November 2016 to May 2017. Moreover, the normal slip (the SE block is relatively subsiding towards the NW block) and thrust (the SE block is relatively uplifting towards the NW block) changed several times during the monitored period; however, the normal slip is dominant (Fig. 3).

4.2. FAULT SLIP KINEMATICS ANALYSES (Fig. 3)

The data recorded on faults TRA1-TRA3 show several individual slips of maximal intensity <0.1 mm/event. All of the recorded slips were marked as events (e.g. E1B) when the time sequence was taken into the account. Based on the orientation of the principal axis calculated for every individual event, the episodes with a predominant pressure (P) or extension (T) regime were delineated (marked as P1 or T2). The first pressure episode (P1), which caused intensive dilatation on fault TRA1, occurred between May 2014 and October 2014. This was followed by a short extensional episode (T1) in the period between October 2014 and November 2015. A longer period of dilatation, between August 2014 and January 2015, was recorded on fault TRA2. Afterwards, the pressure episode (P2) between November 2014 and March 2015 occurred. During this episode, an intensive contraction on fault TRA3 and an intensive dilatation on fault TRA1 were recorded. After this episode, the extension regime occurred on all three faults between March 2015 and June 2015. The weaker short pressure phase (P3) was recoded on faults TRA1 and TRA3 between June 2015 and Jul 2015 and more an intensive short pressure phase (P4) occurred between October 2017 and November 2017. During this period, an intensive contraction on fault TRA3 was recorded. It is evident that the intensity of the slips was higher between the beginning of the measurement in April 2014 until June 2015, and also at the end of 2016. These episodes were more-or-less synchronously recorded on all three of the monitored faults. The other slips were less intensive, took a shorter period of time and were very often not present on all of the monitored faults. There were also five events (marked as *), which were not assigned to any episode.

It can be concluded that the orientation of the slips on the monitored faults changed during the study period.

4.3. FAULT SLIP DYNAMICS ANALYSES (Fig. 4)

Based on the kinematic data set, three different pressure and two extension phases were recognised and the parameters of the stress tensors were calculated. All of the data are presented in Table 1, and the calculated parameters of the current stress tensors for the individual phases are presented in Table 2.

Compression phase P-f1

This compression phase was constructed based on eight kinematic data sets. It is characterised as a reverse slip recorded on all of the monitored faults.

The orientation of the principal axis is subhorizontal *σ1* (6°/18° after FaultKin7 or 24°/29° after ROCK2014; trend/plunge) and subvertical *σ3* (232°/65° or 235°/57°). The maximum shear stress planes are oriented 129°/60° to the NE (strike/dip) as reverse faults and 37°/14° to the SE as reverse faults, with the opening fissures oriented 145°/33° to the NE. This phase was observed on fault TRA1 during the periods 22 May 2014 – 18 October 2014 and 7 October 2016 – 14 November 2016; on fault TRA2 during the periods 22 May 2014 – 29 August 2014 and 15 January 2015 – 14 March 2015; and on fault TRA3 during the periods 17 November 2014 – 14 March 2015, 22 June 2015 – 23 June 2015 and 03 November 2016 – 19 November 2016.

Compression phase P-f2

This compression phase was constructed based on seven kinematic data sets and was recorded on fault TRA1 as a normal slip and TRA3 as a reverse slip. It is characterised by subhorizontal *σ1* (312°/26° or 293°/22°) and also subhorizontal *σ3* (222°/1° or 212°/39°). The maximum shear stress planes are oriented 92°/47° to S as normal faults and 156°/72° to SW as reverse faults, opening fissures are oriented 129°/55° to SW. This phase was recorded on fault TRA1 during the periods 17 November 2014 – 14 March 2015, 01 January 2016 – 03 January 2016, 22 January 2016 – 23 January 2016 and 29 May 2017-30 May 2017; on fault TRA3 during the periods 29 August 2014 – 17 November 2014 and 06 June 2015 – 16 June 2015.

Compression phase P-f3

This compression phase was constructed based on only four kinematic data sets and was recorded on faults TRA1 and TRA3 as a reverse slip. It is very similar to the P-f2 phase. The orientations of the principal axes are *σ1* (125°/6° or 107°/18°) and *σ3* (224°/59° or 212°/39°). The planes with the maximal shear stress are oriented 153°/67° to the NE and 79°/45° to the N, both as reverse faults. The opening fissures are oriented 122°/51° to the NE.

Extension phase T-f1

This extension phase was constructed based on eight kinematic data sets and was recorded as a normal slip on all of the monitored faults. It is characterised by subhorizontal *σ3* in direction (304°/1° or 270°/1°) and subvertical *σ1* (211°/64° or 180°/44°). The maximum shear stress planes are oriented 159°/70° to the NE as a normal slip and 22°/71° to the NW as a normal slip. The opening fissures are oriented 0°/89° to the E. This phase was observed on fault TRA1 during the periods 18 October 2014 – 17 November 2014, 08 August 2015 – 11 August 2015 and 03 January 2016 – 09 January 2016; on fault TRA2 during the periods 18 October 2014 – 15 January 2015, 14 March 2015 – 15 April 2015 and on fault TRA3 during the periods 14 March 2015 – 02 April 2015, 10 November 2016 – 14 November 2016 and 16 September 2017 – 17 September 2017.

Extension phase T-f2

This extension phase was constructed based on six kinematic data sets. It is characterised by subhorizontal *σ3*, which is rotated more to the NNW (286°/31°) in comparison with the very similar extension phase T-f1. This orientation of the stress field causes a normal slip on faults TRA2, TRA3 and a reverse slip on TRA1. The maximum shear stress planes are oriented 32°/85° to the SE as a reverse slip and 171°/37° to the E as a normal slip. The opening fissures are oriented 16°/59° to the E. It was observed on fault TRA1 during the period from 14 March 2015 – 05 May 2015, on fault TRA2 during the periods 29 August 2014 – 18 October 2014 and 01 May 2015 – 24 June 2015, on fault TRA3 during the periods 18 October 2014 – 17 November 2014, 15 January 2015 – 14 March 2015, 09 October 2015-14 October 2015 and 19 September 2016 – 06 October 2016.

It can be concluded that the stress parameters, calculated for the slip, indicate switching of compression and extension phases.

4.4. STRESS FIELD BEHAVIOUR

Most of the works dealing with the mechanism of brittle tectonic processes is based on a generalised elastic deformation model (e.g. Ramsay and Huber, 1987; Ramsay and Lisle, 2000), which assumes a straightforward link between stress and deformation as a cause and consequence. According to this model, the switching of slip orientation on the studied faults gives evidence of switching of the stress states that generate these slips. The recorded slips show that the orientation of the slips on the monitored faults changed during the study period.

4.4.1. COMPRESSIONS AND THEIR PARAMETERS AND ORIGIN

The participation of two compressional stress states was identified: an NNE-orientated compression marked as π1 including the compression phase P-f1 (Fig. 4) and a WNW to NW-orientated compression marked as π2. The latter appears in the form of two close compression phases (P-f2 and P-f3), with slightly differing orientations of *σ2* and *σ3* (Fig. 4). This can be associated with either a gradual re-orientation of the stress field during the deformation or, on the contrary, with the rotation of the deformation block against the stable stress field (Angelier, 1989).

In the event of a tectonic origin, the computed present-day stress field orientation within the DG should be similar to the orientations discovered so far in the broader region, most of which are registered in the World Stress Map (Heidbach et al., 2016 in Fig. 5). Based on the data from the World Stress Map,

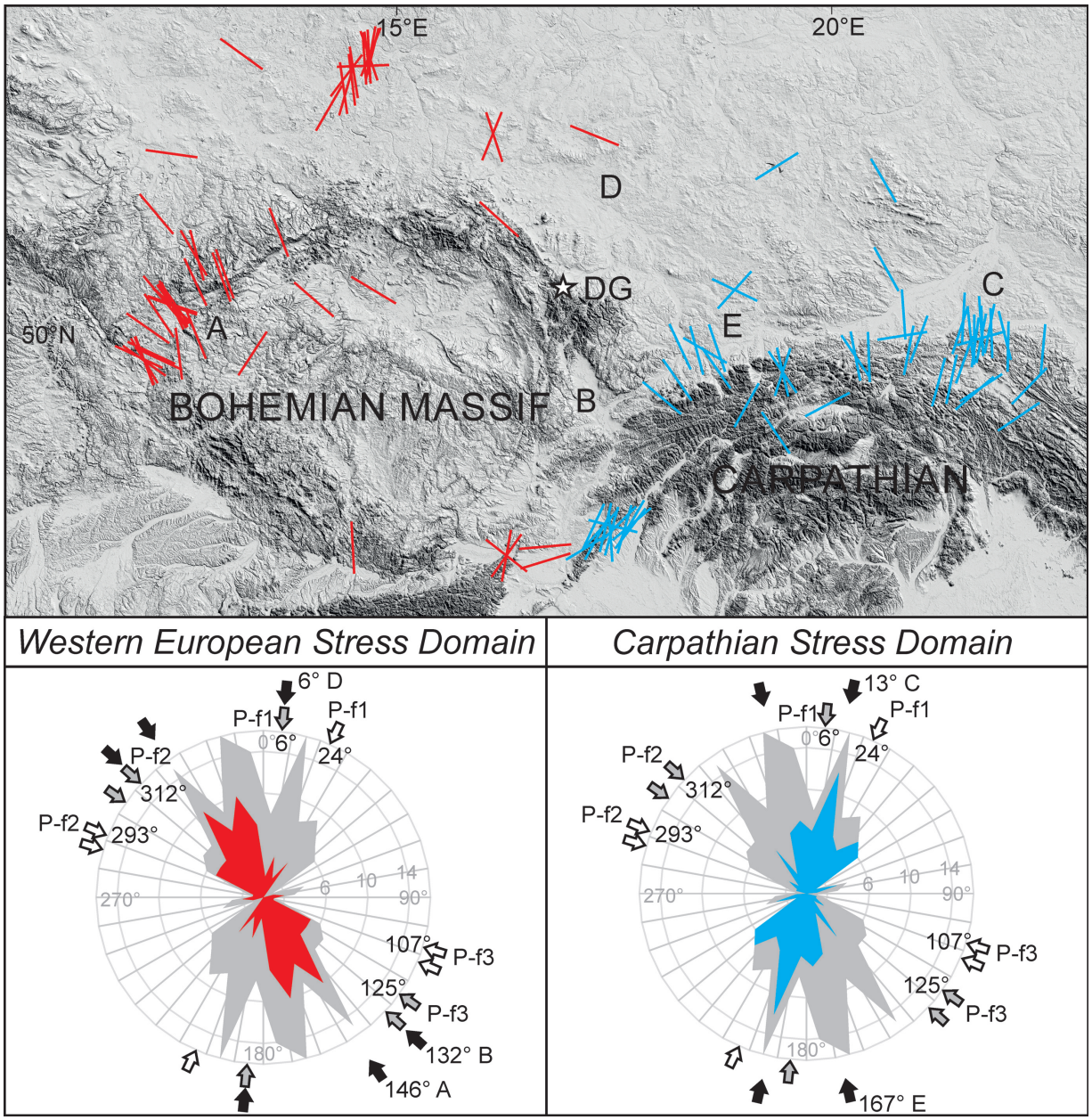

Fig. 5 Orientation of compressions compared with other published works.
Radar plots show orientation of compressions based on World Stress Map 2016 (Heidbach et al., 2016) in cumulative count, divided to groups after azimuth 10°. Red dihedra show orientations of compression determined in Bohemian Massif region and its northern foreland, blue dihedra show orientations of compression determined in Carpathian region and its foreland.
White arrows:
Orientation of compression based on ROCK2014 solution in individual tectonic phases (P-f1, P-f2 and P-f3)
Gray arrows:
Orientation of compression based on FaultKin7 solution in individual tectonic phases
Black arrows:
A – orientation of compression after Vavryčuk et al. (2013) in western Bohemia
B – orientation of compression after Špaček et al. (2006) in Moravia region
C – orientation of compression after Jarosiński et al. (2006) in Malopolski region
D – orientation of compression after Jarosiński et al. (2006) in Foresudetic block region
E – orientation of compression after Jarosiński et al. (2006) in Upper Silesian Massif region
DG – the Dědičná štola Gallery

two distinct provinces are present in the broader region. The Western European stress domain (Müller et al., 1992), covers the W and NW parts of the Central European Platform, including the Bohemian Massif. It is predominantly influenced by a NW-SE oriented compression as a product of spreading of the North-Atlantic ridge (Grünthal and Stromeyer, 1992; Müller et al., 1992; Peška, 1992; Zoback, 1992; Jarosiński et al., 2006; Vavryčuk et al., 2013; Špaček et al., 2015). The Carpathian stress domain (Jarosiński, 2005) is governed by the overall fan-like stress pattern with a predominant NNE-SSW to N-S oriented compression. The origin of this compression is in the tectonic push of the Western Carpathians, mainly – the ALCAPA microplate, as a continued convergence of Africa-Arabia and Europe (Grünthal and Stromeyer, 1992; Müller et al., 1992; Zoback, 1992; Jarosiński, 2005; Jarosiński et al., 2006). It is evident that two different stress orientations were recorded during a short period of nearly four years in the DG. We assume that these are different manifestations of the current geodynamic processes in two different provinces. The study region is situated in the border area between both provinces, where the influence of both could be manifested simultaneously. These phenomena were observed and described in Grünthal and Stromeyer (1992) in the Lower Rhine Graben area, by Dèzes et al. (2004) in the Upper Rhine Graben and by Jarosiński et al. (2006) in the Polish Carpathians.

4.4.2. EXTENSIONS AND THEIR PARAMETERS AND ORIGIN

The second stress state, which participates in the recorded slip, is a generally WNW-orientated extension ($\tau 1$). As for the compression stress state $\pi 2$, the extension stress state is represented by two very close stress phases (T-f1 and T-f2). Theoretically, the origin of the extensions could clearly be tectonic or could be affected by gravitational creeping of the subsurface rock blocks or other slope mass movements. The tectonic origin of the ~E-W extension on the border of the two different stress provinces (mentioned previously) can be derived from the results based on the models presented in Grünthal and Stromeyer (1994). The theory of gravitationally creeping surface rock blocks is supported by the opened cracks near the entrance to the DG (the first 8 m), whereas deeper in the massif the cracks are closed. The nearby slope orientation mainly dips to 100°, and in general (mountain ridge) to 70°. Nevertheless, there is no evidence of the presence of slope deformations (landslides, etc.) corresponding to the exogenous phenomena, these extension states may likely correspond to gravitational spreading as a reaction to mountain ridge uplift. Similarly, it corresponds to the monitored slips (creeping of subsurface blocks) of the uplifting rock massif described in the Outer Western Carpathians by Stemberk et al. (2017).

4.4.3. POTENTIALLY REACTIVATED FAULTS AND THEIR SPATIAL DISTRIBUTION (Fig. 6)

The faults in Figure 6 were supplemented by several morpholineaments (e.g. Abdullah et al., 2010; Badura et al., 2003; Štěpančíková et al., 2008). A DEM based on a LIDAR dataset with a resolution of 1pt/1sqm (CODGiK, 2014 – Poland; DMR-5g ČÚZK, 2016 – Czechia) was used for the identification. Only morpholineaments longer than 1 km were considered. Additionally, the spatial distribution of springs, swamps, deepened riverbeds and their linear arrangement to the morpholineaments was used for more precise delineation. This information was used during the geomorphological mapping.

Based on the LIDAR DEM, several morpholineaments were recognised within study area. Due to their morphological expression, they were considered as unknown faults (further marked as faults in Fig. 6). The structural geological analysis theoretically shows the most reactivated fault planes with the maximal shear-stress (Fig. 4), which is well-oriented to the stress field during the individual stress-phases. According to Skácel (1963) and Ivan (1966), most of the faults in the broader area are nearly sub-vertical, but the fault dip orientation and angle are unknown. We approximate the problem of the reactivation of the faults to the distribution of the fault strikes only, where the dip angle and dip direction were not considered (Fig. 4). The activity of the individual fault segments was evaluated based on the number of stress-phases when the fault segment could have been potentially activated.

It is concluded that the most potentially reactivated faults are striking 340°-350° (potentially reactivated during four stress phases) and striking between 320°-340° and 20°-40° (potentially reactivated during three phases). The sense of movement on these faults and morpholineaments depends on the dip direction, which is unknown for the majority of the faults. The spatial distribution (Fig. 6) indicates the concentration of potentially reactivated faults in the SMF zone and in the Kamenička Fault zone (KF), several faults, parallel to the SMF zone, are concentrated around a nameless hill at elevation 543 m and several faults are present in the area of Zálesí village. Some potentially reactivated faults are also present in the Travná depression. These faults are very often followed by watercourses and the activity of these faults causes enhanced erosion in their beds (Fig. 6) and may determine their longitudinal profiles (c.f. Štěpančíková and Stemberk, 2016).

5. DISCUSSION

The recorded fault slips may reflect exogenous as well as endogenous processes.

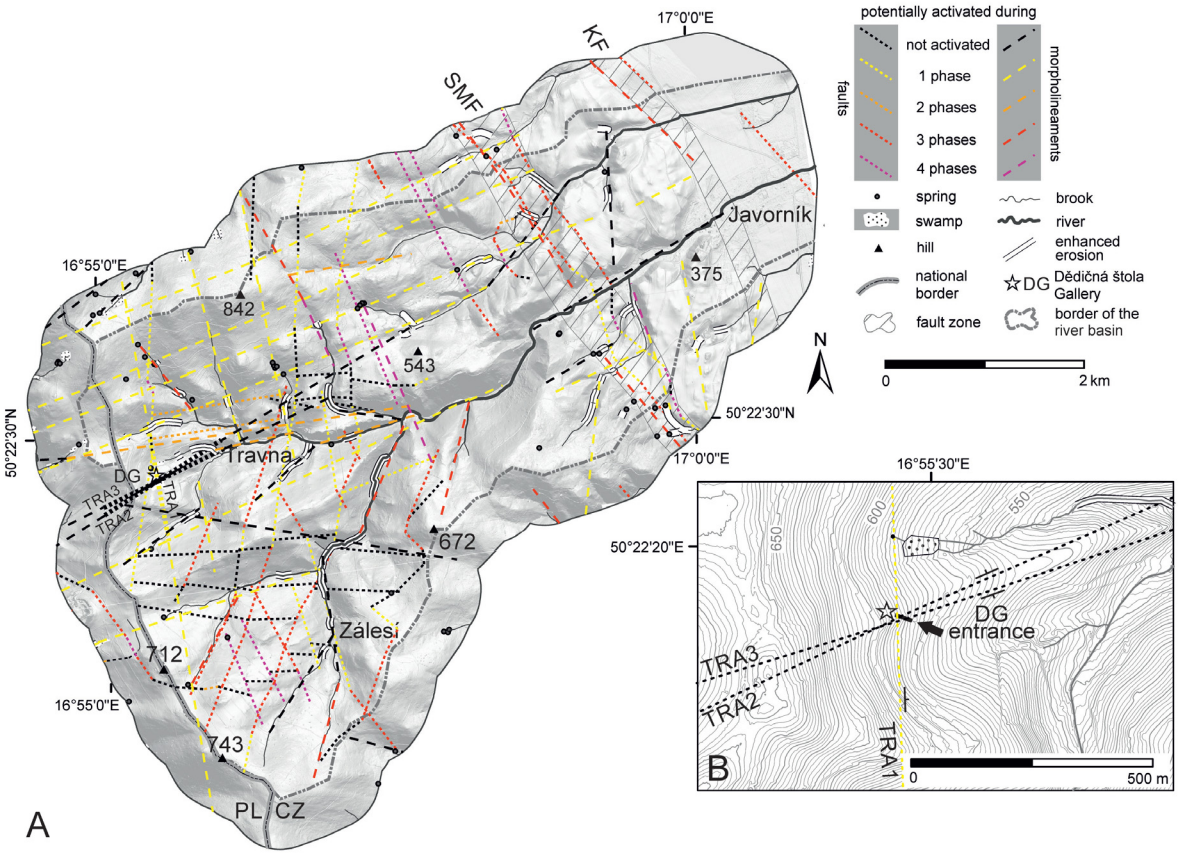

Fig. 6 A – The relief map of Travná depression with observed faults, other published faults and morpholineaments; Consider the spatial distribution of potentially activated faults/morpholineaments striking 340°-350° (potentially activated during 4 stress phases) and striking between 320°-340°and 20°-40° (potentially active during 3 phases) and enhanced erosion concentred in SMF zone, KF zone, around faults parallel to SMF and faults around Zálesí village.
B – Detail relief map around the Dědičná štola Gallery.

5.1. EXOGENOUS INFLUENCES

There are several exogenous processes that may potentially affect the measurements, the most significant of which are thermo-elastic effects due to yearly temperature changes and surface movements such as e.g. landslides or rock sliding.

5.1.1. TEMPERATURE INFLUENCES

The position of the extensometers in the gallery significantly reduces the effects of yearly temperature changes as well as direct sunlight. According to Gosar et al. (2009) and Briestenský et al. (2010), the seasonal amplitude of opening/closing components due to thermo-elastic deformation across the fault is less than 0.05 mm at depths of more than 10 m. The seasonal temperature changes ranged around 4°C due to very low air circulation in the DG.

The thermo-elastic effect affects not only the rock massif itself but the components of the instrument as well (Briestenský et al., 2010). The dilatation and contraction of the TM-71 extensometers is analytically computed and systematically removed.

As can be seen in Figure 3, some repeated slips along the p-axis (the most sensitive to temperature changes and the thermo-elastic fault contraction and dilatation) were recorded. Nevertheless, regular yearly changes cannot be detected from the fault slip records. It can be concluded that the thermo-elastic effect, if any, is less than the sensitivity of the extensometers.

5.1.2. SURFACE PROCESSES

The DG is situated in the central part of steep slope inclined to the ESE by about 20° (Figs. 2 and 6). According to the landslide inventory map of the Rychlebské hory Mts. compiled by the Czech Geological Survey (mapy.geology.cz) and our field investigation, there is no evidence of significant indicators of gravitational slope movements affecting just the monitored site or the vicinity of the DG. Due to position of the DG on the steep slope, the influence of precipitation on the recorded events as well as possible deep-seated slope deformation processes were studied using monthly rainfall data for the period from January 2014 to December 2017 (Fig. 3). Data

used in the analysis were provided by the Czech Hydrometeorological Institute from the Javorník meteorological observatory (portal.chmi.cz). The monthly average precipitation between 2007 and 2017 reached about 55 mm. The mean annual precipitation in the studied period (2014-2017) reached about 600 mm.

To investigate the possible influence of precipitation on the slip events recorded in the gallery, the differences between monthly cumulated precipitation and long-term monthly average were calculated. This method was firstly used by Záruba and Mencl (1982) and applied for landslide activity in different regions. The rising part of the curve represents the wet period, which is prone to landslide acceleration, while the decreasing trend shows dry periods. For the studied period, three wet periods can be identified. The first one started in May 2014 and ended in October 2014, the second wet period started in June 2016 and ended in August 2016 and the third wet period started in April 2017 and ended in November 2017. Nevertheless, there is no significant correlation between wet periods and recorded fault slips.

Analysis of the meteorological data shows an extreme precipitation period around September 2014 (Fig. 3), when water saturation of the massif was unambiguously higher than usually. During this period, slips in a scale ≈0.1 mm were recorded. Extreme rainfall events with intensity ≥20 mm/24h (bold date ≥ 40 mm/24h) occurred on 23 March 2014, 16-17 May 2014, **28 May 2014, 26 June 2014,** 30 June 2014, 11 July 2014, **01 September 2014,** 11 September 2014, 23 October 2014, 13 June 2015, 09 April 2016, 13 June 2016, **26 July 2016,** 21 August 2016, 04 October 2016, 28 April 2017, 24 July 2017, 11 August 2017 and **01 September 2017**.

Moreover, no extreme rainfalls correlated to the recorded fault slip. The correspondence of the recorded movement and the extreme rainfall seem to be random. This indicates that there is no direct relationship between extreme rainfall and the slips on the monitored faults.

Therefore, it can be concluded that the recorded normal slip events were not influenced by gravitational movements triggered by precipitation.

5.2. ENDOGENOUS EFFECTS

The main endogenous process, which could potentially affect the measurement, is seismicity in broader area.

5.2.1. SEISMICITY

Analysis of natural earthquakes recorded by the IPE-MONET seismic network (Sýkorová et al., 2018) indicates changes in earthquake occurrence during the period between 2014 and 2017. The more active period between January 2014 and February 2015 was followed by a period with lower earthquake occurrence between March 2015 and September 2017. Between September 2017 and December 2017, the occurrence of earthquakes increased again (Fig. 3, Table 3). It can be concluded that this significant irregularity in earthquake distribution during the studied period corresponds to the recorded higher intensity of fault slips in the period between April 2014 and June 2015.

Table 3 Sum of earthquakes recorded by IPE-MONET seismic network during the period 2014-2017 (after Sýkorová et al., 2018)

Year	Sum of earthquakes
2014	217
2015	140
2016	135
2017	201

5.3. RESULT OF MONITORING AT OTHER SITES (EU-TECNET NETWORK)

The extensometers placed in the DG is included in the EU-TecNet network, which is, using the same methodology, focused on long-term monitoring of fault slips in different parts of Europe. The number of monitored sites, more than one hundred and fifty, spreads across the globe allows us to compare the results from the DG with published results from different parts of the network. It was discovered that periods of increased fault slip activity occur contemporaneously along distinct tectonic units (Stemberk et al., 2010; Briestenský et al., 2015).

Briestenský et al. (2015) reported that simultaneous short-lasting transtensional faulting occurred between 2013 and 2015 at sites in the eastern part of the Western Carpathians. The most significant fault slips occurred in the first half of 2015. As the authors concluded, many of the monitored sites in other regions of the European plate (e.g. northern sites in Spitsbergen as well as southern sites in Greece) recorded evidence of a simultaneous fault slip anomaly in the second half of 2014 / beginning of 2015, which is interpreted to reflect the occurrence of a tectonic pressure pulse towards the second half of 2014. Similarly, the most intensive fault slips were also recorded at the turn of 2014-2015 in the DG.

The cause is assumed to be the wide-spread transient short-term redistribution of stress/strain within the crust, which resulted in transient fault re-activations. This conclusion is supported by their synchronous onset on more faults in distant regions of Europe at the turn of 2014-2015, as well as a higher occurrence of earthquakes.

6. CONCLUSION

Analysis of the kinematics and dynamics of the fault displacements recorded in the Dědičná štola Gallery over the last four years revealed that the sub-horizontal orientation of the dominant principal stresses in both the compression and extension

regimes indicates a tectonic origin of the recorded fault slips and a pulse regime with alternating periods of compression and extension.

The present-day stress field corresponding to the monitored fault slips switches in two compression modes: WNW-ESE to NW-SE compression corresponding to the stress field of the Western European stress domain, and NNE-SSW corresponding to the stress field of the NW part of the Carpathian stress domain. On the contrary, the extensional regime has a NW-SE orientation and corresponds to gravitational spreading due to the uplift of the Rychlebské hory Mts.

Potentially activated faults by the current stress field strike 340-350°, 320°-340° and 20°-40°. Faults with corresponding strikes were recognised in the SMF zone, KF zone as well as near Zálesí village. Faults of these strikes are morphologically dominant.

ACKNOWLEDGEMENT

This research was carried out in the framework of the infrastructural project CzechGeo/EPOS No. LM 2010008 (2010 – 2015) and No. LM 2015079 since 2016 and the project CzechGeo/EPOS - Sci CZ.02.1.01/0.0/0.0/16_013/0001800. This study was conducted thanks to the support of the long-term conceptual development research organization RVO: 67985891.

REFERENCES

Abdullah, A., Akhir, J.M. and Abdullah, I.: 2010, Automatic mapping of lineaments using shaded relief images derived from digital elevation model (DEMs) in the Maran Sungi Lembing Area, Malaysia. Electron. J. Geotech. Eng., 15J, 949–957.

Aleksandrowski, P. and Mazur, S.: 2002, Collage tectonics in the northeasternmost part of the Variscan Belt: the Sudetes, Bohemian Massif. In: Winchester, J., Pharaoh, T. and Verniers, J. (Eds.): Palaeozoic Amalgamation of Central Europe. Geological Society, London, Special Publications, 201, 237–277. DOI: 10.1144/GSL.SP.2002.201.01.12

Allmendinger, R.W., Cardozo, N.C. and Fisher, D.: 2011, Structural Geology Algorithms: Vectors & Tensors. Cambridge, England, Cambridge University Press, 289 pp. DOI: 10.1017/CBO9780511920202

Angelier, J.: 1989, From orientation to magnitudes in paleostress determination using fault slip data. J. Struct. Geol., 11, 37–50. DOI: 10.1016/0191-8141(89)90034-5

Angelier, J.: 1994, Fault slip analysis and palaeostress construction. In: Hancock, P. L. (Ed.): 1994, Continental Deformation. Pergamon Press, 53–100. DOI: 10.1017/S001675680001160

Angelier, J., Tarantola, A., Valette, B. and Manoussis, S.: 1982, Inversion of field data in fault tectonics to obtain the regional stress - 1. Single phase fault populations: a new method of computing the stress tensor. Geophys. J. Int., 69, 3, 607–621. DOI: 10.1111/j.1365-246X.1982.tb02766.x

Badura, J., Zuchiewicz, W., Górecki, A., Sroka, W., Przybylski, B. and Żyszkowska, M.: 2003, Morphotectonic properties of the Sudetic Marginal Fault, SW Poland. Acta Montana, Series A, 24, (131), 21–49.

Baroň, I., Plan, L., Sokol, L., Grasemann, B., Melichar, R., Mitrovic, I. and Stemberk, J.: 2019, Present-day kinematic behaviour of active faults in the Eastern Alps. Tectonophysics, 752, 1–23. DOI: 10.1016/j.tecto.2018.12.024

Bobula, I.: 1968, Povrchová geologická mapa okolí ložiska 1:10 000 (Surface geological map of deposit and its surrounding in scale 1:10 000). Geofond Dolní Rožínka, (in Czech).

Brezňan, J. (Ed.): 1957a, Geologická mapa M-33-58-D (Bílá Voda) 1:50 000 (Geological map M-33-58-D (Bílá Voda)). Czechoslovak Uranium Survey, Příbram, (in Czech).

Brezňan, J. (Ed.): 1957b, Geologická mapa M-33-59-C (Javorník) 1:50 000 (Geological map M-33-59-C (Javorník)). Czechoslovak Uranium Survey, Příbram, (in Czech).

Briestenský, M., Košťák, B., Stemberk, J., Petro, L., Vozár, J. and Fojtíková, L.: 2010, Active tectonic fault microdisplacement analyses: A comparison of results from surface and underground monitoring in western Slovakia. Acta Geodyn. Geomater., 7, 4, 387–397.

Briestenský, M., Hochmuth, Z., Littva, J., Hók, J., Dobrovič, R., Stemberk, J., Petro, L. and Bella, P.: 2018, Present-day stress orientation and tectonic pulses registered in caves of the Slovenský kras Mts (south-eastern Slovakia). Acta Geodyn. Geomater., 15, 2, 93–103. DOI: 10.13168/AGG.2018.0007

Briestenský, M., Rowberry, M. D., Stemberk, J., Stefanov, P., Vozár, J., Šebela. S., Petro, L., Bella, P., Gaal, L. and Orkumov, C.: 2015, Evidence of a plate-wide tectonic pressure pulse provided by extensometric monitoring in the Balkan Mountains (Bulgaria). Geol. Carpath., 66, 5, 427–438. DOI: 10.1515/geoca-2015-0035

Coubal, M., Málek, J., Adamovič, J. and Štěpančíková, P.: 2015, Late Cretaceous and Cenozoic dynamics of the Bohemian Massif inferred from the paleostress history of the Lusatian Fault Belt. J. Geodyn., 87, 26–49. DOI: 10.1016/j.jog.2015.02.006

Dèzes, P., Shmid, S.M. and Ziegler, P.A.: 2004, Evolution of the European Cenozoic Rift System: interaction of the Alpine and Pyrenean orogens with their foreland lithosphere. Tectonophysics, 389, 1–33. DOI: 10.1016/j.tecto.2004.06.011

Don, J., Skácel, J. and Gotowała, R.: 2003, The boundary zone of the East and West Sudetes on the 1:50 000 scale geological map of the Velké Vrbno, Staré Město and Śnieżnik Metamorphic Units. Geol. Sudetica, 35, 25–59.

Dyjor, S.: 1983, Evolution of Tertiary grabens situated before Central and Eastern Sudetes. Mater. III Kraj. Symp. "Współczesne i neotektoniczne ruchy skorupy ziemskiej w Polsce" (3rd Regional Conference "Modern and neotectonic movements of the Earth crust in Poland"), IV. Publishing.

Fossen, H.: 2010, Structure Geology. Cambridge University Press, New York, 463 pp. DOI: 10.1017/CBO9780511777806

Franke, W. and Żelaźniewicz, A.: 2000, The eastern termination of the Variscides: terrane correlation and kinematic evolution. In: Franke, W., Haak, V., Oncken, O. and Tanner, D. (Eds.): Orogenic processes: Quantification and modelling in the Variscan Belt. Geological Society, London, Special

Publications, 179, 63–86.
DOI: 10.1144/GSL.SP.2000.179.01.06

Gosar, A., Šebela, S., Košťák, B. and Stemberk, J.: 2009, Surface versus underground measurement of activity displacement detected with TM 71 extensometers in western Slovenia. Acta Carsologica, 38, 2-3, 213–226.

Grünthal, G. and Stromeyer, D.: 1992, The recent crustal stress field in Central Europe: Trajectories and finite element modelling. J. Geophys. Res., 97, (B8), 11805–11820. DOI: 10.1029/91JB01963

Grünthal, G. and Stromeyer, D.: 1994, The recent crustal stress field in Central Europe sensu lato and its quantitative modelling. Geologie en Mijnbouw, 73, 173–180.

Havíř, J., Pazdírková, J., Skácelová, Z. and Sýkorová, Z.: 2001, Tektonická mikrozemětřesení registrovaná na Moravě a ve Slezsku v roce 2000 (Tectonic micro-earthquakes recorded in Moravia and Silesia in year 2000). Geologické výzkumy na Moravě a ve Slezsku (Geological research in Moravia and Silesia), 7, 105–108, (in Czech).

Heidbach, O., Rajabi, M., Reiter, K., Ziegler, M. and WSM Team: 2016, World Stress Map Database Release 2016. GFZ Data Services.
DOI: 10.5880/WSM.2016.001

Hippolyte, J.-C., Bergerat, F., Gordon, M., Bellier, O. and Espurt, N.: 2012, Keys and pitfalls in mesoscale fault analysis and paleostress reconstructions, the use of Angelier's methods. Tectonophysics, 581, 144–162. DOI: 10.1016/j.tecto.2012.01.012

Ivan, A.: 1966, Geomorfologické poměry severozápadní části Rychlebských hor, Kandidátská práce (Geomorphological conditions of NW part of the Rychlebské hory Mts, Ph.D. theses). Geological Institute of the Czechoslovak Academy of Sciences, Brno, 120 pp., (in Czech).

Ivan, A.: 1997, Topography of the Marginal Sudetic Fault in the Rychlebské hory Mts. and geomorphological aspects of epiplatform orogenesis in the NE part of Bohemian Massif. Morav. Geogr. Rep., 5, 3–17.

Jarosiński, M.: 2005, Ongoing tectonic reactivation of the Outer Carpathians and its impact on the foreland: Result of borehole breakout measurement in Poland. Tectonophysics, 410, 189–216.
DOI: 10.1016/j.tecto.2004.12.040

Jarosiński, M.: 2006, Recent tectonic stress field investigations in Poland: a state of the art. Geol. Q., 50, 3, 303–321. DOI: 10.7306/gq.v50i3.7415

Jarosiński, M., Beekman, F., Bada, G. and Cloetingh, S.: 2006, Redistribution of the recent collision push and ridge push in Central Europe: Insight from FEM modelling. Geophys. J. Int., 167, 860–880.
DOI: 10.1111/j.1365-246X.2006.02979.x

Klimeš, J., Rowberry, M. D., Blahůt, J., Briestenský, M., Hartvich, F., Košťák, B., Rybář, J., Stemberk, J. and Štěpančíková, P.: 2012, The monitoring of slow-moving landslides and assessment of stabilisation measures using an optical–mechanical crack gauge. Landslides, 9, 3, 407–415.
DOI: 10.1007/s10346-011-0306-4

Košťák, B.: 1969, A new device for in situ movement detection and measurement. Exp. Mechanics, 9, 8, 374–379.

Košťák, B.: 2006, Deformation effects in rock massifs and their long-term monitoring. Q. J. Eng. Geol. Hydroge., 39, 3, 249–258. DOI: 10.1144/1470-9236/05-024

Kroner, U., Mansy, J.-L., Mazur, S., Aleksandrowski, P., Hann, H.P., Huckriede, H., Lacquement, F., Lamarche, J., Ledru, P., Pharaoh, T.C., Zedler, H., Zeh, A. and Zulauf, G.: 2008, Variscan tectonics. In: McCann, T. (Ed.): The geology of Central Europe. The Geological Society, London, 599–664.
DOI: 10.1144/CEV1P.11

Krzyszkowski, D., Migoń, P. and Sroka, W.: 1995, Neotectonic Quaternary history of the Sudetic Marginal fault, SW Poland. Folia Quaternaria, 66, 73–98.

Málek, J., Fischer, T. and Coubal, M.: 1991, Computation of regional stress tensor from small scale tectonic data. Publ. Inst. Geophys. Pol. Acad. Sci., M-15, 235, 77–92.

Marrett, R.A., and Allmendinger, R.W.: 1990, Kinematic analysis of fault-slip data. J. Struct. Geol., 12, 973–986. DOI: 10.1016/0191-8141(90)90093-E

Martí, X., Rowberry, M.D. and Blahůt, J.: 2013, A MATLAB (R) code for counting the moiré interference fringes recorded by the optical-mechanical crack gauge TM-71. Comput. Geosci.-UK, 52, 164-167. DOI: 10.1016/j.cageo.2012.09.029

Mazur, S., Aleksandrowski, P., Kryza, R. and Oberc-Dziedzic, T.: 2006, The Variscan Orogen in Poland. Geol. Q., 50, 1, 89–118.

Morris, A., Ferrill, D. A. and Henderson, D.B.: 1996, Slip-tendency analysis and fault reactivation. Geology, 24, 3, 275–278.
DOI: 10.1130/0091-7613(1996)024

Müller, B., Zoback, M.I., Fuchs, K., Mastin, I., Gregersen, S., Pavoni, N., Stephansson, O. and Liunggren, C.: 1992, Regional patterns of tectonic stress in Europe. J. Geophys. Res., 97, B8, 11783–11803.
DOI: 10.1029/91JB01096

Müller, V. and Čurda, J.: 2003, Vysvětlivky k souboru geologických a ekologických účelových map přírodních zdrojů v měřítku 1:50 000, Listy 04-43, 04-44, 14-21, 14-22, Bílý Potok, Javorník, Travná, Jeseník. (Legend to collection of geological and environmental map of natural resources in scale 1:50 000, sheets 04-43, 04-44, 14-21, 14-22, Bílý potok, Javorník, Travná, Jeseník). Czech Geological Survey, Prague, 80 pp., (in Czech).

Oberc, J.: 1972, Tektonika, część 2 (Tectonics, part 2). In: Pożaryski, W. (Ed.): Budowa Geologiczna Polski t. IV (Geological structure of Poland, part IV). Geological Publishing, Warszawa, 307 pp, (in Polish).

Oberc, J. and Dyjor, S.: 1969, Marginal Sudetic Fault.o, 236, 41–142, (in Polish).

Ondra, P. and Potměšil, O.: 1965, Geologická mapa Javornického výběžku 1:25 000 (Geological map of the Javorník region in scale 1:25 000), Geofond, (in Czech).

Pagaczewski, J.: 1972, Catalogue of earthquakes in Poland in 1000–1970 years. Publs. Inst. Geoph. Pol. Acad. Sc., 51, 3–36.

Pecina, V., Čurda, J., Hanáček, M., Kočandrle, J., Nývlt, D., Opletal, M., Skácelová, D., Skácelová, Z., Večeřa, J. and Žáček, V.: 2005, Základní geologická mapa České republiky 1 : 25 000 s vysvětlivkami list 14–221 Žulová (Geological map of the Czech Republic in scale 1:25 000 with legend, sheet 14-221 Žulová). Czech Geological Survey, Praha. Geofond, (in Czech).

Peška, P.: 1992, Stress indications in the Bohemian Massif: reinterpretation of borehole televiewer data. Stud. Geophys. Geod., 36, 4, 307–324. DOI: 10.1007/BF0162548

Ramsay, J.G. and Huber, M.I.: 1987, The technique of modern structural geology, Volume 2: Folds and fractures. Academic Press, London, 309–697. DOI: 10.1017/S0016756800010384

Ramsay, J.G. and Lisle, R.J.: 2000: The technique of modern structural geology, Volume 3: Application of continuum mechanics in structure geology. Academic Press, London, 560 pp.

Skácel, J.: 1963, Geologie krystalinika a rudních výskytů ve střední části Rychlebských hor (Geology of the crystalline complex and ore in central part of the Rychlebské hory Mts). J. Geol. Sci., 3, 109–139, (in Czech).

Skácel, J.: 1989, Křížení okrajového zlomu lugika a Nýznerovského dislokačního pásma mezi Vápennou a Javorníkem ve Slezsku (Intersection of the marginal Lugicum fault and Nýznerov dislocation zone between Vápenná and Javorník). Geographica - Geologica, 95, 31–45, (in Czech).

Skácelová, D. (Ed.): 1992, Geologická mapa ČR, 1:50 000, list 14-21 Travná (Geological map of the Czech Republic on scale 1:50 000, sheet 14-21 Travná). Czech Geological Survey, Prague, (in Czech).

Skácelová, Z. and Havíř, J.: 1999, Earthquakes on the eastern margin of the Bohemian Massif recorded by the stations of the IPE Brno. EGRSE J., 2, 16–21.

Stemberk, J., Košťák, B. and Cacoń, S.: 2010, A tectonic pressure pulse and increased geodynamic activity recorded from the long-term monitoring of faults in Europe. Tectonophysics, 487, 1–12. DOI: 10.1016/j.tecto.2010.03.001

Stemberk, J., Hartvich, F., Blahůt, J., Rybář, J. and Krejčí, O.: 2017, Tectonic strain changes affecting the development of deep seated gravitational slope deformations in the Bohemian Massif and Outer Western Carpathians. Geomorphology, 289, 3–17. DOI: 10.1016/j.geomorph.2016.07.004

Stemberk, J., Dal Moro, G., Stemberk, J. jr., Blahůt, J., Coubal, M., Košťák, B., Zambrano, M. and Tondi, E.: 2019, Strain monitoring of active faults in the central Apennines (Italy) during the period 2002-2017. Tectonophysics, 750, 22–35. DOI: 10.1016/j.tecto.2018.10.033

Sýkorová, Z., Pazdírková, J., Zacherle, P., Špaček, P. and Vlach, R.: 2018, IPE-MONET earthquake catalog. IPE Masaryk University Brno. DOI: 10.14470/Z6115722

Špaček, P., Sýkorová, Z., Pazdírková, J., Švancara, J. and Havíř, J.: 2006, Present-day seismicity of the south-eastern Elbe Fault System (NE Bohemian Massif). Stud. Geophys. Geod., 50, 2, 233–258. DOI: 10.1007/s11200-006-0014-z

Špaček, P., Zacherle, P., Sýkorová, Z., Pazdírková, J. and Havíř J.: 2008, Microseismic activity of the Upper Morava Basin and surroundings. Journal of scientific works – construction series, Technical University of Ostrava, 8, 2, 287–295.

Špaček, P., Bábek, O., Štěpančíková, P., Švancara, J., Pazdírková, J and Sedláček, J.: 2015, The Nysa-Morava Zone: an active tectonic domain with Late Cenozoic sedimentary grabens in the Western Carpathians' foreland (NE Bohemian Massif). Int. J. Earth Sci., 104, 4, 963–990. DOI: 10.1007/s00531-014-1121-7

Štěpančíková, P., Stemberk, J., Vilímek, V. and Košťák, B.: 2008, Neotectonic development of drainage networks in the East Sudeten Mountains and monitoring of recent fault displacements (Czech Republic). Geomorphology, 102, 68–80. DOI: 10.1016/j.geomorph.2007.06.016

Štěpančíková, P. and Stemberk, J. jr.: 2016, Region of the Rychlebské Hory Mountains - Tectonically controlled landforms and unique landscape of granite Inselbergs (Sudetic Mountains). Landscape and landforms of the Czech Republic. Book Series: World Geo-morphological Landscapes, 263–276. DOI: 10.1007/978-3-319-27537-6_21

Vavryčuk, V., Bouchaala, F. and Fischer, T.: 2013, High-resolution fault image from accurate locations and focal mechanisms of the 2008 swarm earthquakes in West Bohemia, Czech Republic. Tectonophysics, 590, 189–195. DOI: 10.1016/j.tecto.2013.01.025

Záruba, Q. and Mencl, V.: 1982, Landslides and Their Control. Development in Geotechnical Engineering, 31, Elsevier Science, 324 pp.

Zedník, J., Bouškova, A. and Pazdírková, J.: 2013, Seismic activity in the Czech Republic in 2011. Stud. Geophys. Geod., 57, 3, 535–542. DOI: 10.1007/s11200-013-0700-6

Zoback, M. L.: 1992, Stress-field constraints on intraplate seismicity in eastern North America. J. Geophys. Res. – Solid Earth, 97, B8, 11761–11782. DOI: 10.1029/92JB00221

Website references:

http://www.tecnet.cz, Accessed date: 14 Feb 2019. http://mapy.geology.cz, Accessed date: 10 Feb 2019. http://portal.chmi.cz, Accessed date: 12 Feb 2019. http://www.codgik.gov.pl, Accessed date: 10 Nov 2017. http://geoportal.cuzk.cz, Accessed date: 8 Nov 2017. https://www2.jpl.nasa.gov/srtm, Farr, T. G., eds.: 2007, The Shuttle Radar Topography Mission. Rev. Geophys., 45, RG2004. DOI: 10.1029/2005RG000183, Accessed date: 12 Apr 2018.